Copper deficiency disrupts OXPHOS and mitochondrial dynamics through MTCH2-dependent copper trafficking in skeletal muscle

Young-Seung Lee[1,2,10], Hee Soo Kim[3,4,10], Phuc L. Nguyen[1,2], Junhyeong Lee[5], Dong-Il Kim[5], Jeongmin Lee[2,5], Changjong Moon[2,5], Kyoung-Oh Cho[2,5], Byung-Eun Kim[6,7], Jiyun Ahn[3,4], Timothy F. Osborne[8], Taner Duysak[2,9], Jeong-Sun Kim[2,9,*], Chang Hwa Jung[3,4,*], and Tae-Il Jeon[1,2,11,*]

[1]Department of Animal Science, Chonnam National University, Gwangju, Republic of Korea
[2]Host-Directed Antiviral Research Center, Chonnam National University, Gwangju, Republic of Korea
[3]Aging and Metabolism Research Group, Korea Food Research Institute, Wanju-gun, Jeollabuk-do, Republic of Korea.
[4]Department of Food Biotechnology, University of Science and Technology, Wanju-gun, Jeollabuk-do, Republic of Korea.
[5]College of Veterinary Medicine, Chonnam National University, Gwangju, Republic of Korea
[6]Department of Animal and Avian Sciences, University of Maryland, College Park, Maryland, USA.
[7]Biological Sciences Graduate Program, University of Maryland, College Park, Maryland, USA
[8]Institute for Fundamental Biomedical Research, Department of Medicine and Biological Chemistry, Johns Hopkin University School of Medicine, St. Petersburg, Florida, USA
[9]Department of Chemistry, Chonnam National University, Gwangju, Republic of Korea;
[10]These authors contributed equally
[11]Lead contact

***Correspondence:**
* Dr. Tae-Il Jeon, Department of Animal Science, College of Agriculture & Life Sciences, Chonnam National University, 77 Yongbong-ro, Buk-gu, Gwangju 61186, Republic of Korea.
E-mail: tjeon@jnu.ac.kr, **Office:** +82-62-530-2127, **Fax:** +82-62-530-2129

* Dr. Chang Hwa Jung, Aging and Metabolism Research Group, Korea Food Research Institute, 245 Nongsaengmyeong-ro, Iseo-myeon, Wanju-gun, Jeollabuk-do 55365, Republic of Korea.
E-mail: chjung@kfri.re.kr

* Dr. Jeong-Sun Kim, Department of Chemistry, College of Natural Sciences, Chonnam National University, 77 Yongbong-ro, Buk-gu, Gwangju 61186, Republic of Korea.
E-mail: jsunkim@jnu.ac.kr

Abstract

Copper is an essential trace element required for mitochondrial respiration and cellular metabolism, yet its role in skeletal muscle remains incompletely understood. Here, we show that skeletal muscle-specific deletion of the high-affinity copper importer *Ctr1* (SMKO) in mice leads to copper deficiency, resulting in exercise intolerance, metabolic dysfunction, and hallmarks of mitochondrial myopathy, including ragged-red fibers, lactic acidosis, and aberrant mitochondrial morphology. Copper deficiency disrupted electron transport chain proteome and induced mitochondrial hyperfusion. We identified mitochondrial carrier homolog 2 (MTCH2), an outer mitochondrial membrane protein, as a copper-binding regulator of mitochondrial copper distribution and morphology. Restoring copper levels via the copper ionophore or AAV-mediated *Ctr1* re-expression rescued mitochondrial function and alleviated myopathic features in SMKO. These findings highlight MTCH2 as a key mediator of a critical link between copper homeostasis and mitochondrial remodeling required for skeletal muscle function.

Keywords: copper; CTR1; mitochondria; MTCH2; myopathy; skeletal muscle

INTRODUCTION

Copper is an essential trace element that supports a wide range of physiological processes. In addition to serving as a cofactor for metabolic enzymes, copper directly contributes to signaling pathways that regulate cell growth, differentiation, and survival[1,2]. Because both copper deficiency and excess can impair these essential functions and contribute to human disease, systemic and cellular copper levels must be tightly controlled. Copper homeostasis is maintained through dietary intake and regulated transport systems[3]. In mammals, dietary copper is absorbed in the intestine and exported into the bloodstream by ATP7A copper-transporting ATPase[4]. Circulating copper is imported into cells via high-affinity copper transporter 1 (CTR1) and distributed by intracellular copper chaperones such as antioxidant 1 (ATOX1), which delivers copper to ATP7A and ATP7B in the trans-Golgi network to support cuproenzyme biosynthesis[5]. Under conditions of copper excess, ATP7A and ATP7B relocate to the plasma membrane or vesicles, respectively, to facilitate copper export, thereby preventing copper toxicity[6,7].

CTR1 is the only known copper-specific importer in mammals and is broadly expressed and localized to the plasma membrane, where it facilitates constitutive copper uptake under physiological conditions[5]. Genetic deletion of CTR1 causes severe developmental defects: intestinal-specific deletion of *Ctr1* in mice leads to perinatal lethality due to systemic copper deficiency[8], and cardiac-specific knockout results in progressive cardiomyopathy and premature death[9]. These findings underscore the essential role of CTR1 in systemic and tissue-specific copper homeostasis.

Skeletal muscle comprises approximately 40% of total body mass and a major site in systemic energy metabolism[10,11]. It is composed of distinct myofiber subtypes: oxidative (slow-twitch) fibers, which are mitochondria-rich and specialized for sustained endurance activities through oxidative phosphorylation (OXPHOS), and glycolytic (fast-twitch) fibers, which rely on glycolysis to generate energy for short bursts of activity[12,13]. Accordingly, mitochondrial function is a critical determinant of muscle performance, and its impairment contributes to diverse myopathies[14-17]. Copper is required for electron transport chain (ETC) function, particularly through assembly and activity of cytochrome c oxidase (COX, Complex IV)[18,19]. Moreover, copper deficiency has also been associated with altered mitochondrial morphology, including increased expression of fusion proteins mitofusin (MFN) 2 and optic atrophy protein 1 (OPA1), although the underlying mechanisms remain unclear[20].

Skeletal muscle contains approximately 27% of total body copper and muscle weakness is a hallmark of inherited copper transport disorders such as Menkes disease.[21,22] However, the physiological role of copper in mature skeletal muscle, particularly during exercise, remains poorly understood. *In vitro* studies have shown that both copper import via CTR1 and mitochondrial uptake via inner membrane transporter SLC25A3 are required for myogenic differentiation and COX activity[23,24]. However, whether copper uptake is essential for skeletal muscle function *in vivo*, particularly through mitochondrial regulation, is unknown.

Here, we show that skeletal muscle-specific *Ctr1* knockout (SMKO) mice exhibit severe copper deficiency, leading to impaired OXPHOS and reduced type IIB muscle fibers, mitochondrial hyperfusion, and progressive myopathy. Mechanistically, we identified mitochondrial carrier homolog 2 (MTCH2), an outer mitochondrial membrane (OMM) protein, as a copper-binding regulator of mitochondrial morphology and copper trafficking. Copper restoration via the copper ionophore elesclomol (ES) or adeno-associated virus (AAV)-mediated *Ctr1* re-expression rescues mitochondrial function and maintains muscle integrity in SMKO mice. These findings reveal a critical role for copper homeostasis in mitochondrial remodeling and skeletal muscle maintenance and identify MTCH2 as a molecular link connecting copper availability and mitochondrial dynamics.

RESULTS

Copper uptake into skeletal muscle contributes to exercise performance

To evaluate the role of copper in exercise performance, we measured copper levels in the gastrocnemius (GA) muscle of wild-type chow-fed mice following four weeks of treadmill training. Copper levels in the GA muscle were significantly elevated in the exercised group compared to sedentary controls (Fig. 1a), whereas levels of other trace metals–including iron, zinc, and manganese–remained largely unchanged despite a slight upward trend (Extended Data Fig. 1). This suggests that copper may play a key role during exercise training. CTR1 is the primary transporter mediating cellular copper uptake, so we generated skeletal muscle-specific *Ctr1* knockout (SMKO) mice by crossing *Ctr1*-floxed mice (Floxed) with myosin light chain 1 (*Myl1*)-Cre transgenic mice to directly evaluate the role of copper in skeletal muscle function. Efficient *Ctr1* deletion in SMKO muscle was confirmed by genomic excision and mRNA expression analyses (Extended Data Fig. 2a-c). Despite comparable body weight and skeletal muscle mass between SMKO and control mice (Extended Data Fig. 2d,e), SMKO mice displayed both reduced grip strength and endurance exercise capacity, along with significantly

124 decreased copper levels in skeletal muscle (Fig. 1b-d). These results suggest that adequate
125 copper uptake into skeletal muscle is important for maintaining muscle strength and exercise
126 tolerance.
127
128 **Copper deficiency in skeletal muscle reduces systemic energy expenditure via a glycolytic**
129 **shift**
130 Exercise capacity is often linked to the ratio of slow-twitch to fast-twitch muscle fibers,
131 with a higher proportion of slow-twitch fibers generally enhancing endurance[14]. Unexpectedly,
132 SMKO mice exhibited a greater proportion of slow-twitch fibers in the GA muscle compared
133 to Floxed controls. Morphologically, SMKO muscles appeared redder, consistent with
134 increased slow-twitch fiber density (Fig. 2a). Myosin heavy chain (MyHC) isoform staining
135 confirmed a shift toward type I and type IIa fibers (Fig. 2b), further supported by upregulation
136 of *Myh7* (type I) and *Myh2* (type IIa), along with downregulation of *Myh1* (type IIx) and *Myh4*
137 (type IIb) at the mRNA level (Fig. 2c). In addition, SMKO myofibers displayed significantly
138 smaller cross-sectional area (CSA) (Fig. 2d). Although muscle atrophy or degeneration can
139 reduce CSA, histological analysis via H&E staining showed no pathological abnormalities
140 (Extended Data Fig. 3a), suggesting that the reduced CSA may reflect a transition to smaller-
141 caliber slow-twitch fibers[25].
142 Since slow-twitch enrichment is typically associated with increased endurance and
143 elevated energy expenditure[14], we next assessed systemic metabolism using indirect
144 calorimetry. Despite the fiber-type shift, SMKO mice showed significantly reduced oxygen
145 consumption (VO_2), with no significant change in carbon dioxide production (VCO_2)
146 (Extended Data Fig. 3b,c), resulting in lower total energy expenditure (Fig. 2e). As reduced
147 VO_2 may indicate impaired mitochondrial bioenergetics[26], we performed Seahorse XF Mito
148 Stress testing on isolated GA myofibers and primary myoblasts. Compared to Floxed controls,
149 SMKO mice exhibited markedly reduced basal and maximal respiration (Fig. 2f and Extended
150 Data Fig. 3d), along with decreased ATP levels (Fig. 2g), indicating impaired OXPHOS within
151 the ETC. To evaluate whether glycolysis compensates for the decline in mitochondrial
152 respiration, we measured extracellular acidification in *Ctr1*-knockdown C2C12 myoblasts.
153 Glycolytic flux was significantly elevated compared to controls (Fig. 2h). Additionally, SMKO
154 mice exhibited increased blood lactate levels (Fig. 2i), further supporting a metabolic shift
155 toward glycolysis. Together, these findings suggest that copper deficiency in skeletal muscle
156 compromises mitochondrial respiration and contributes to metabolic reprogramming toward

157 glycolysis, ultimately resulting in reduced systemic energy expenditure and impaired exercise
158 performance.
159
160 **Copper deficiency alters mitochondrial ETC balance and promotes features of**
161 **mitochondrial myopathy**
162 To explore the mechanisms underlying mitochondrial dysfunction in SMKO muscle,
163 we performed proteomic analysis of GA tissue from Floxed and SMKO mice. Using a fold-
164 change cutoff of 1.5 and an adjusted p value < 0.05, we identified 88 differentially expressed
165 proteins (DEPs), comprising 53 upregulated and 35 downregulated proteins in SMKO muscle,
166 as shown in the volcano plot (Fig. 3a). A substantial proportion of DEPs were mitochondrial
167 proteins associated with OXPHOS (Fig. 3b,c). Gene ontology (GO) analysis revealed that most
168 of the downregulated proteins in SMKO muscle were involved in Complex IV of the ETC,
169 particularly in electron transfer from cytochrome c to oxygen (Fig. 3d). In contrast, upregulated
170 proteins were enriched in pathways related to Complexes I and II, as well as ATP synthesis, as
171 shown in the heatmap analysis (Fig. 3e and Extended Data Fig. 4). The most significantly
172 downregulated proteins were cytochrome c oxidase subunit 1 (MTCO1/COX1) and
173 MTCO2/COX2, both of which are copper-binding proteins critical for Complex IV function[27].
174 Western blot analysis confirmed a marked reduction in Complex IV in SMKO muscle,
175 accompanied by compensatory upregulation of other ETC complexes and copper chaperone
176 for superoxide dismutase (CCS), which is commonly induced under copper-deficient
177 conditions (Fig. 3f)[28,29].
178 Mitochondrial myopathy (MM) is characterized by mitochondrial dysfunction,
179 involving impaired respiration and mutations in mitochondrial DNA[16,30]. MM is frequently
180 associated with Complex IV deficiency, Complex II upregulation, and elevated blood lactate
181 levels[31]. Given the striking phenotypic similarity, we hypothesized that *Ctr1* deletion in skeletal
182 muscle might promote a pathology resembling MM. In support of this, SMKO mice exhibited
183 severe MM-like features, including increased succinate dehydrogenase (SDH) activity, ragged-
184 red fibers, and enlarged, morphologically abnormal mitochondria (Fig. 3g,h). Analysis of a
185 human GEO dataset further revealed that *CTR1* transcript levels were significantly reduced in
186 muscle biopsies from MM patients compared to healthy controls (Fig. 3i).
187 To examine whether the observed metabolic and histopathological changes are sex-
188 dependent, we evaluated exercise performance and muscle pathology in female SMKO mice.
189 Similar to males, female SMKO mice exhibited reduced exercise capacity (Extended Data Fig.

190 5a,b), along with elevated SDH and ragged-red fibers, but without increased blood lactate
191 levels (Extended Data Fig. 5c,d), suggesting that these MM-like phenotypes occur
192 independently of sex. Together, these findings suggest that copper deficiency in skeletal muscle
193 disrupts mitochondrial ETC balance and induces molecular and histological hallmarks of MM.
194

195 **Copper directly binds to MTCH2 and regulates its stability**

196 Building on our proteomic analysis of SMKO muscle, we next sought to identify
197 candidate copper-binding proteins that could contribute to mitochondrial dysfunction under
198 copper deficiency. Among the 88 DEPs, analysis with a metal-binding prediction tool
199 MeBiPred[32] identified six potential copper-binding candidates, including the canonical COX
200 subunits MTCO1 and MTCO2 (Extended Data Fig. 6a). We next focused on mitochondrial
201 carrier homolog 2 (MTCH2, SLC25A50) because of its predicted Cu^+ specificity, OMM
202 localization, and previously described roles in mitochondrial apoptosis, dynamics, and
203 OXPHOS regulation[33-35]. In vitro metal-binding assay revealed that MTCH2 selectively bound
204 to copper-charged resin, but not to iron-, zinc-, or uncharged resins, with dose-dependent
205 affinity (Fig. 4a). To investigate the structural basis of this interaction, we modeled the
206 theoretical structure of MTCH2 using AlphaFold 3, as its experimental structure remains
207 unresolved. The predicted model features an open α-barrel and a bulky region comprising
208 several α-helices and two β-strands located at one end of the β-barrel (Fig. 4b). Polar and
209 hydrophilic residues line the barrel's interior, and numerous hydrophobic residues are
210 externally exposed, consistent with its integration in the lipid bilayer[36]. This model revealed
211 that the barrel's internal surface is unusually exposed to the lipid bilayer (highlighted by the
212 red dotted circle in Fig. 4b, left panel), a feature rarely observed in experimentally determined
213 protein structures. To identify a closed α-barrel with similar folding, a structural similarity
214 search was conducted using the DALI server (Liisa Holm,
215 http://ekhidna2.biocenter.helsinki.fi/dali). This search, using the AlphaFold-predicted MTCH2
216 structure, retrieved structural homologs (PDB ID 8J1N, mitochondrial brown fat uncoupling
217 protein; PDB IDs 1OKC and 4C9H, mitochondrial ADP/ATP carrier proteins) with Z-scores
218 greater than 20[37,38]. These homologs feature a closed α-barrel with flexible surrounding regions
219 and superimpose on the AlphaFold-predicted open MTCH2 structure with a root-mean-square
220 deviation (RMSD) of less than 3.1 Å. Furthermore, these homologs contain various lipids
221 surrounding the α-barrel, demonstrating their role as membrane proteins. Using the ADP/ATP
222 carrier protein structure (PDB ID 1OKC, SLC25A4) as a template, a refined MTCH2 structure

223 was generated using SWISS MODEL[39]. In this model, the open α-barrel is closed by
224 incorporating a helix formed by the C-terminal residues (N282-Y295, referred to as the C-helix,
225 Fig. 4b, middle panel) into the α-barrel. By integrating the sequence features of MTCH2 with
226 the structural information derived from the modeled structures, we identified two sets of
227 candidate copper-binding regions: sulfur-rich residues (M244, C268, M278) located on the
228 exterior of the α-barrel, and nitrogen- and oxygen-rich residues (H142, R185, S241; H88, E127,
229 R131) lining the barrel's interior (Fig. 4b, right panel). To validate these predictions, we
230 generated alanine substitution mutants at these positions and assessed their copper-binding
231 capacity. Notably, the M244A, C268A, and M278A mutants exhibited significantly reduced
232 copper binding, indicating that these residues are critical for MTCH2-copper interaction (Fig.
233 4c and Extended Data Fig. 6b).
234 Because copper often regulates protein stability, and MTCH2 was ~1.8-fold
235 upregulated in SMKO muscle (Extended Data Fig. 6a), we next examined whether MTCH2
236 undergoes copper-dependent turnover. In *Mtch2*-KO C2C12 myoblasts re-expressing MTCH2-
237 WT, $CuSO_4$ treatment led to a dose-dependent reduction in MTCH2 stability (Fig. 4d). This
238 degradation was blocked by MG132, consistent with proteasome-mediated regulation[40].
239 Importantly, excess copper selectively reduced MTCH2-WT levels, whereas the copper-
240 binding–deficient M244A mutant remained unaffected (Fig. 4e). These results demonstrate that
241 copper directly binds MTCH2 via a binding site containing critical sulfur-rich residues and that
242 copper regulates MTCH2 stability through a proteasome-mediated mechanism.
243
244 **MTCH2 coordinates mitochondrial dynamics with copper trafficking**
245 Given that copper directly regulates MTCH2 stability, we next examined whether its
246 functional roles are influenced by copper availability. MTCH2 is well known for promoting
247 mitochondrial fusion[33,41], and the hyperfused morphology of SMKO muscle suggested a link
248 between copper status, MTCH2, and mitochondrial fusion dynamics. Consistent with this,
249 copper chelation with bathocuproinedisulfonic acid (BCS) induced mitochondrial elongation
250 consistent with increased fusion (Extended Data Fig. 7a), as previously reported[20]. In line with
251 this, mitochondria isolated from SMKO quadriceps (Quad) showed increased levels of the
252 fusion proteins MFN2 and OPA1, together with MTCH2, without changes in fission markers
253 (Fig. 5a). Consistent with prior reports[33,41], *Mtch2* knockdown induced mitochondrial
254 fragmentation (Fig. 5b). Notably, BCS-induced elongation was abolished in *Mtch2*-silenced
255 C2C12 cells, demonstrating that MTCH2 is required for mitochondrial hyperfusion under

256 copper-deficient conditions (Fig. 5b). We next tested whether copper overload, which
257 destabilizes MTCH2, would compromise this function. In *Mtch2*-KO C2C12 myoblasts, re-
258 expression of either MTCH2-WT or the copper-binding–deficient M244A mutant rescued
259 mitochondrial elongation, indicating that copper-binding is dispensable for its role in fusion
260 (Fig. 5c). However, under copper overload, MTCH2-WT was destabilized and degraded,
261 resulting in mitochondrial fragmentation, whereas the M244A mutant resisted degradation and
262 preserved elongated mitochondria (Fig. 5c), suggesting that copper binding to M244 is a critical
263 determinant of MTCH2 stability and its role in maintaining mitochondrial morphology.
264 Beyond its role in dynamics, MTCH2 is localized to the OMM and belongs to the
265 SLC25 family of metabolite carriers[42,43]. Because copper overload commonly triggers
266 transporter degradation to limit toxic accumulation[44], we hypothesized that MTCH2 may also
267 contribute to copper trafficking. Supporting this, both MTCH2 and the inner-membrane copper
268 transporter SLC25A3 were upregulated by BCS-induced copper depletion across multiple cell
269 lines (Fig. 5d and Extended Data Fig. 7b). Silencing *Mtch2* significantly reduced mitochondrial
270 copper levels under copper-replete–but not basal–conditions (Fig. 5e), and impaired Complex
271 IV expression and mitochondrial copper accumulation during myogenic differentiation (Fig.
272 5f). Moreover, re-expression of MTCH2-WT in *Mtch2*-KO myoblasts restored COX1 levels,
273 whereas copper-binding mutant the M244A failed to do so (Fig. 5g). Together, these findings
274 identify MTCH2 as a dual-function protein: it enables mitochondrial hyperfusion as an
275 adaptive response to copper deficiency and likely facilitates copper trafficking at the outer
276 membrane to sustain Complex IV activity. These dual roles suggest that MTCH2 integrates
277 copper status with both mitochondrial integrity and respiratory function.
278
279 **The copper ionophore elesclomol (ES) restores exercise capacity and mitochondrial**
280 **function in SMKO mice**
281 ES is a copper ionophore that facilitates intracellular copper delivery independently of
282 CTR1, thereby supporting COX activity and improving viability in copper-deficient yeast and
283 cell models[45,46]. Notably, ES has also been shown to rescue mitochondrial function and reduce
284 mortality in a mouse model of Menkes disease[47], raising the possibility that targeted copper
285 supplementation may reverse muscle phenotypes driven by copper deficiency.
286 To test this, we administered ES subcutaneously to SMKO mice for two weeks. ES
287 treatment significantly increased copper levels in the GA muscle and substantially improved
288 exercise capacity in SMKO mice (Fig. 6a,b). Remarkably, ES treatment also reduced the

289 elevated proportion of slow-twitch fibers in SMKO muscles to levels comparable to those in
290 Floxed controls, as evidenced by gross muscle color and immunostaining-based analysis of
291 myofiber composition (Fig. 6c and Extended Data Fig. 8a). This shift in fiber type was
292 accompanied by enhanced mitochondrial respiration in isolated GA single myofibers and
293 reduced blood lactate concentrations (Fig. 6d,e), consistent with a reversal of the glycolytic
294 reprogramming observed in SMKO mice. In line with these findings, ES treatment normalized
295 VO_2 and total energy expenditure to levels observed in Floxed mice (Fig. 6f and Extended Data
296 Fig. 8b). ES also partially restored Complex IV expression in SMKO muscles (Fig. 6g) and
297 ameliorated histopathological features, including myofiber degeneration and mitochondrial
298 ultrastructural abnormalities (Fig. 6h,i). Together, these findings show that pharmacological
299 copper delivery via ES can restore mitochondrial function and improve MM-like phenotypes
300 in SMKO mice. These results underscore the reversibility of copper deficiency–induced
301 myopathy and suggest that ES-mediated copper supplementation may represent a viable
302 approach to restore mitochondrial function under conditions of impaired copper availability.
303

304 **AAV-DIO-mediated restoration of *Ctr1* reverses mitochondrial dysfunction and exercise**
305 **impairments in SMKO mice**

306 AAV vectors are widely utilized for *in vivo* gene delivery, with the AAV9 serotype
307 exhibiting high transduction efficiency in skeletal muscle. To assess whether restoring Ctr1
308 expression could ameliorate the MM-like phenotypes in SMKO mice, we employed a Cre-
309 activated AAV-double-floxed inverted open reading frame (DIO) system to specifically induce
310 *Ctr1* expression in skeletal muscle (Extended Data Fig. 9a). Following systemic AAV2/9
311 administration, *Ctr1* expression was successfully reinstated in SMKO muscle (Extended Data
312 Fig. 9b), resulting in elevated muscle copper levels and improved exercise performance (Fig.
313 7a,b). Myofiber composition analysis revealed normalization of fiber-type distribution, with an
314 increased proportion of fast-twitch fibers in AAV-DIO-*Ctr1*-treated SMKO mice (Fig. 7c and
315 Extended Data Fig. 9c). This was accompanied by enhanced mitochondrial respiration in
316 isolated myofibers, reduced blood lactate levels (Fig. 7d,e), and recovery of whole-body VO_2
317 and total energy expenditure (Fig. 7f and Extended Data Fig. 9d). Furthermore, Complex IV
318 expression and mitochondrial morphology were restored, along with normalized MTCH2
319 levels (Fig. 7g–i). Collectively, these findings indicate that targeted *Ctr1* re-expression is
320 sufficient to re-establish copper homeostasis in skeletal muscle and reverse key metabolic and
321 mitochondrial defects arising from copper deficiency. These results support a mechanistic link

322 between CTR1-dependent copper uptake and mitochondrial function in muscle tissue.
323
324 **DISCUSSION**
325 Mitochondrial function is fundamental to skeletal muscle metabolism, and defects in
326 OXPHOS contribute to muscle weakness and metabolic disorders[48]. Copper, an essential
327 cofactor for COX in Complex IV of the ETC, is indispensable for mitochondrial respiration,
328 yet its regulation and potential role in skeletal muscle physiology has remained poorly
329 understood. Here, we identify a critical role for copper in maintaining mitochondrial integrity
330 and muscle performance through the action of the copper binding OMM protein MTCH2.
331 Skeletal muscle–specific deletion of the copper importer CTR1 produced progressive copper
332 deficiency and a myopathic phenotype characterized by impaired exercise capacity, ETC
333 proteome imbalance, OXPHOS dysfunction, and systemic metabolic deficits.
334 Mitochondrial copper homeostasis has been primarily attributed to the inner membrane
335 carrier SLC25A3, which imports copper into the matrix to sustain COX activity[49,50]. While
336 copper can traverse the OMM when bound to apo-ligand[51], the molecular mediators of this
337 process remained unclear. Several mitochondrial proteins predicted to bind copper were
338 differentially regulated in SMKO mice, including MTCH2, an OMM protein of the SLC25
339 family. We show that MTCH2 binds copper directly through a motif characterized by a cluster
340 of sulfur containing amino acids. We further show that MTCH2 deletion reduced mitochondrial
341 copper content and COX expression in myoblasts, and copper-binding–deficient MTCH2
342 mutants failed to restore COX1, supporting its role in copper trafficking. Copper status also
343 influenced mitochondrial morphology, which is a previously reported role of MTCH2.
344 Adequate copper supports COX activity and triggers mitochondrial "flickering"—transient
345 depolarization events that activate the metalloendopeptidase OMA1, leading to OPA1 cleavage
346 and thereby restraining fusion[52]. Under copper-deficient conditions, flickering is suppressed,
347 OPA1 remains intact, and mitochondria undergo hyperfusion. Consistent with this, copper
348 depletion triggered hyperfusion in myoblasts, an effect abolished by MTCH2 knockdown.
349 Conversely, copper overload destabilizes MTCH2, leading to fragmentation in part by reducing
350 its pro-fusion activity. These observations reveal a previously unrecognized dual role for
351 MTCH2 in the dynamics of copper-deficiency-induced mitochondrial fusion.
352 Interestingly, previous work reported that skeletal muscle-specific deletion of MTCH2
353 enhances mitochondrial respiration, promotes oxidative fiber type switching, and improves
354 exercise performance[35,53]. At first glance, this appears contradictory to our finding that MTCH2

355 facilitates mitochondrial copper delivery to support Complex IV. If MTCH2 loss reduces
356 mitochondrial copper content, one would expect impaired COX activity and hyperfusion,
357 resembling copper deficiency. Instead, MTCH2 KO muscle displays increased respiration and
358 mitochondrial fragmentation, more like copper overload where MTCH2 is destabilized. A
359 possible explanation for the differences with our study relates to the dual roles for MTCH2 and
360 to possible compensatory pathways, such as CTR1-mediated uptake or alternative copper
361 carriers, that preserve mitochondrial copper under basal conditions. This would sustain COX
362 activity and flickering. Indeed, this is supported by our finding that mitochondrial copper levels
363 remain unchanged under basal conditions, even in the absence of MTCH2. In this context, loss
364 of MTCH2's pro-fusion function would result in fragmentation. By contrast, in our studies,
365 CTR1 deletion would eliminate copper availability and prevent MTCH2 from contributing to
366 copper trafficking. However, our studies show that MTCH2 protein is stabilized under copper
367 deficiency which would promote hyperfusion while OXPHOS collapses. These contrasting
368 phenotypes coupled with MTCH2's differing roles in copper deficiency vs overload highlights
369 that its contribution to copper homeostasis is highly context dependent, becoming critical when
370 copper flux is stressed. Direct quantification of mitochondrial copper pools and COX activity
371 in MTCH2 KO muscle will be essential to disentangle these dual influences of MTCH2 on
372 copper homeostasis and mitochondrial morphology.

373 Our findings also underscore the importance of maintaining copper homeostasis in
374 mature skeletal muscle. While copper has been previously implicated in myoblast proliferation
375 and differentiation[23,24], our study extends this understanding by showing that mitochondrial
376 copper regulation is essential for sustaining metabolic and structural integrity in skeletal muscle
377 mitochondria. This has important implications for muscle-related diseases, including MM and
378 sarcopenia, in which metabolic decline and ETC dysfunction are common pathological
379 features[31,54]. Reduced exercise capacity is also a hallmark of Menkes disease–a systemic copper
380 deficiency disorder caused by mutations in ATP7A[47]–and has been observed in amyotrophic
381 lateral sclerosis models with superoxide dismutase [Cu-Zn] mutations[55,56]. In both contexts,
382 copper imbalance may contribute to impaired mitochondrial function and reduced endurance.

383 Therapeutically, our data show that restoring copper availability can effectively reverse
384 mitochondrial and metabolic dysfunction in copper-deficient muscle. Treatment with ES, a
385 copper ionophore that bypasses CTR1-mediated transport, restored copper levels, rescued
386 OXPHOS activity, and improved exercise capacity in SMKO mice. Likewise, AAV-mediated
387 re-expression of *Ctr1* restored mitochondrial function and metabolic balance. These findings

388 highlight that both pharmacological and gene therapy strategies can restore copper homeostasis
389 in muscle. With AAV9 already in clinical use for neuromuscular disorders and expanding
390 interest in metabolic myopathies[16,57-59], targeting copper regulation may represent a promising
391 and underexplored approach.
392 In conclusion, this study identifies CTR1 and MTCH2 as key regulators of
393 mitochondrial copper homeostasis in mitochondrial function in skeletal muscle. This study also
394 reveals that MTCH2 is a dual-function protein that coordinates copper delivery and integrates
395 copper status with mitochondrial dynamics. These findings reveal a previously unrecognized
396 mechanistic link between copper metabolism, mitochondrial structure, and muscle
397 performance, providing new perspectives on the pathophysiology of copper imbalance and its
398 therapeutic targeting in a wide range of muscular disorders.
399
400 **Methods**
401 **Animals**
402 The *Ctr1* skeletal muscle-specific knockout (SMKO) mice were generated by crossing
403 $Ctr1^{flox/flox}$ mice[8] with Myl1/mlc1f-Cre transgenic mice ($Myl1^{tm1(cre)sjb}$/J; Jackson Laboratory,
404 024713). All mice were housed at 22°C under a 12-hour dark–light cycle and given free access
405 to food and water. For the elesclomol (ES) (MedChemExpress, STA-4783) rescue experiment,
406 mice were subcutaneously (s.c.) injected with 10 mg kg^{-1} $body^{-1}$ weight ES in 0.5% Methocel™
407 (final 2% DMSO) for 2 weeks. For the adeno-associated virus (AAV) injection, mice were
408 anesthetized using an intraperitoneal injection of avertin (Sigma-Aldrich, T48402). Mice were
409 intramuscularly and s.c. injected with 5×10^{12} AAV viral particles (Vp) in 50 µl of PBS, then
410 subjected to an experiment 5-week post-injection. All animal experiments were performed in
411 accordance with accepted standards of animal protection welfare and with permission from the
412 Institutional of Animal Care and Use Committees at the Chonnam National University (YB-
413 2021-59, YB-2022-90, YB-2023-164) and Korea Food Research Institute (KFRI-M-23043).
414
415 **Cell lines, differentiation, and transfection**
416 C2C12 murine myoblast (ATCC, CRL-1772™), HEK293T (ATCC, CRL-11268™),
417 Huh7 (ATCC, PTA-4583), HeLa (ATCC, CCL-2™), and A549 (ATCC, CCL-185™) cells were
418 purchased from the American Type Culture Collection and Human skeletal muscle myoblast
419 cells (HSMM) from Lonza (CC-2580). C2C12, HEK293T, Huh7, HeLa, and A549 cells were
420 cultured in Dulbecco's modified Eagle medium (DMEM)/high glucose (HyClone, SH30243.01)

421 supplemented with 10% FBS (HyClone, SH30919.03), 100 U ml^{-1} penicillin, and 100 μg ml^{-1}
422 streptomycin (Gibco, Thermo Fischer, 15140122). HSMM cells were cultured in skGM™-2
423 Skeletal Muscle Cell Growth Medium-2 BulletKit™ (Lonza). C2C12 myoblasts were
424 differentiated into myotubes using DMEM/high glucose supplemented with 2% horse serum
425 (Sigma Aldrich, H1138), 100 U ml^{-1} penicillin, and 100 μg ml^{-1} streptomycin. C2C12
426 myoblasts were transfected with small interfering RNA targeting mouse *Ctr1*, *Mtch2*, or
427 negative control (Bioneer) for 48 h using TransIT-X2® Transfection Reagent (Takara Bio Inc.)
428 according to manufacturer's instructions. C2C12 myoblasts and HEK293T cells were
429 transfected for 24 h with MTCH2 WT, MTCH2 mutants plasmids using PolyJet™ In Vitro
430 DNA Transfection reagent (SignaGen).

431

432 **CRISPR/Cas9-mediated *Mtch2* Knockout cell generation**

433 Single guide RNAs (sgRNAs) targeting Mtch2 were designed using the GenScript CRISPR
434 gRNA Design Tool (https://www.genscript.com/tools/gRNA-design-tool). The selected gRNA
435 oligonucleotides were synthesized, annealed, and cloned into the Esp3I-digested
436 lentiCRISPRv2 (Addgene, Plasmid #52961). For lentivirus production, HEK293T cells were
437 seeded in 6 cm dishes. On the following day, the medium was replaced with Opti-MEM
438 supplemented with 5% FBS, 30 minutes prior to transfection. Cells were co-transfected with 1
439 μg each of lentiCRISPRv2 (either control or gRNA-containing), psPAX2 (Addgene, Plasmid
440 #12260), and pCMV-VSV-G (Addgene, Plasmid #8454) using Lipofectamine 3000
441 transfection reagent (ThermoFisher). Six hours after transfection, the medium was replaced,
442 and viral supernatants were harvested at 24h (1st harvest) and 48 h (2nd harvest) post-
443 transfection. The two collections were pooled and filtered through 0.45 μm syringe filter.
444 C2C12 myoblasts were transduced with 2 ml of the filtered viral supernatant supplemented
445 with 10 μg ml^{-1} polybrene (Santa Cruz) and incubated for 4 h. After incubation, an additional
446 2 ml of viral supernatant and 2 ml of fresh growth medium were added, followed by 24 hours
447 of incubation. Puromycin selection was performed by refreshing the 1 μg ml^{-1} puromycin
448 (Sigma-Aldrich)-containing medium daily until all non-transduced cells were eliminated.
449 Surviving cells were then expanded in puromycin-free medium for downstream experiments.
450 For Guide-it CRISPR/Cas9 system (Takara Bio Inc.), gRNA was annealed, and cloned into p-
451 Guide-it-ZsGreen1 vector following the manufacturer's instructions. The gRNA sequence were
452 obtained from a previously reported study[33]. The plasmid constructs were transfected into

453 C2C12 myoblasts, which were seeded into 96 wells plates. Single GFP-positive cells were
454 subsequently selected, and knockout efficiency was confirmed by immunoblotting. gRNA
455 sequences are listed in Supplementary Table 1.

456 **AAV-mediated gene transduction**

457 The mouse *Ctr1* gene (NM_175090) was synthesized by VectorBuilder (VectorBuilder)
458 in a pAAV-double-floxed inverted open-reading frame plasmid and was transfected into 293T
459 cells. Cells containing viral particles were harvested 60 h post-transfection, lysed in AAV lysis
460 buffer (150 mM NaCl, 20 mM Tris pH 8.0), and further incubated with benzonase to remove
461 nucleic acid. The virus supernatant was purified using an iodixanol gradient solution and
462 centrifuged at 280,000 × g and 14℃ for 3 h. The purified viruses were concentrated using the
463 Amicon Ultra-15 Centrifugal Filter Unit (Sigma-Aldrich, UFC9100). The viruses were
464 incubated sequentially with DNase and proteinase K for AAV titration to eliminate any
465 remaining plasmid DNA and protein. The number of Vp was measured using the CFX96 Real-
466 Time PCR system (Bio-Rad).
467

468 **Inductively coupled plasma (ICP) mass spectrometry (MS)**

469 Skeletal muscle tissues were digested with 7 ml of 65% HNO_3 and 1 ml of 30% H_2O_2
470 in a Teflon decomposition container. The mixture was processed using the microwave
471 decomposition sequence (Milestone). After cooling, it was adjusted to 50 ml with 0.1% nitric
472 acid. Samples were analyzed by ICP-MS (PerkinElmer). For cytosolic and mitochondrial
473 copper measurements, samples were mixed with 0.5 ml of 70% HNO_3 and heated at 80℃ for
474 8 h. After cooling to room temperature, the samples were diluted with ultrapure water to a final
475 volume of 10 ml. Amounts of metals were measured using an Agilent 7900 ICP-MS (Agilent)
476 and normalized to cell number.
477

478 **Grip strength test**

479 The forelimb grip strength of mice was measured using the Digital Force Gauge
480 (Shimpo). Mice were allowed to hold on to a metal grid with their fore paws and were gently
481 pulled backward by the tail away from the grid until the mice released their grip. The grip
482 strength test performed 6 consecutive measurements per day at one-minute intervals. The
483 average values of the 6 tests were normalized by body weight and used to represent the grip
484 strength of each mouse.

485

486 **Treadmill test**

487 Mice were acclimatized to the treadmill (Panlab) by performing a 10 m min^{-1} run for
488 30 min for 2 days. The mice were then run on the treadmill at 6 m min^{-1} for the first 5 min
489 followed by increases of 3 m min^{-1} with a 5% incline every 3 min toward 21 m min^{-1} and a 10%
490 incline until exhaustion. Mice were removed from the treadmill after remaining still for 5 sec
491 on the electrical grid continuously, and the running time and distance were recorded.

492

493 **Reverse transcription-quantitative PCR (RT-qPCR)**

494 Total RNA was isolated using TRIzol reagent (Molecular Research Center, Inc.,
495 TR118), and cDNA was synthesized using a ReverTra Ace qPCR RT kit (Toyobo) to analyze
496 mRNA expression. Quantitative PCR was performed with SYBR Green Master Mix
497 (Enzynomics) using a qTOWER3 real-time PCR Thermal Cycler (Analytik Jena). Primer
498 sequences are shown in Supplementary Table 1. Samples were normalized to mouse ribosomal
499 protein, large, P0 (RPLP0), and calculated using the comparative threshold cycle method.

500

501 **Immunoblotting**

502 The cells or mouse skeletal muscles were lysed in RIPA (50 mM Tris, 150 mM NaCl,
503 0.1% SDS, 0.5% sodium deoxycholate, 1% Triton X) containing protease and phosphatase
504 inhibitors (APExBIO, K1007; K1013; K1014). The lysates were incubated on ice for 30 min,
505 further sonicated, and centrifuged at 27,000 × g and 4°C for 20 min. The supernatants were
506 collected, and protein concentrations were measured using the Pierce BCA Protein Assay kit
507 (Thermo Fisher, 23225). Equal amounts of protein were separated on SDS-PAGE gels and
508 transferred to nitrocellulose or PVDF membranes (Pall Corporation). After blocking in 5%
509 skim milk for 1 h, membranes were incubated in primary antibodies at 4°C overnight, followed
510 by incubation with secondary antibodies (Cell signaling technology). The blots were developed
511 using an EZ-Western Lumi Pico or Femto Western Blot Detection kit (DoGenBio) and
512 visualized using the Odyssey XF imaging system (LI-Cor Biosciences). Protein levels were
513 quantified using ImageJ software. Antibodies used in immunoblotting are listed in
514 Supplementary Table 2.

515

516 **Immunofluorescence**

517 Skeletal muscle tissues were embedded in Tissue-Tek OCT Compound (Sakura

518 Finetek, 4583) with liquid nitrogen-cooled isopentane, and 10 μm thick sections were prepared
519 using a cyromicrotome. For immunofluorescence, muscle sections were incubated with M.O.M.
520 IgG blocking solution (Vector Laboratories, MKB-2213-1) and 10% goat serum (Sigma
521 Aldrich, G9023) in PBS at RT for 1 h, then stained with primary antibodies in PBS containing
522 1% BSA at 4°C overnight. After 3 washes with PBS, secondary antibodies were incubated at
523 RT for 1 h and mounted with Vectashield Hardset Antifade mounting medium (Vector
524 Laboratories, H-1400-10) or Slowfade Diamond Antifade mountant with DAPI (Thermo Fisher,
525 S36964). Immunofluorescence images were acquired using the ZEISS LSM 900 confocal
526 microscope (Carl Zeiss). Quantification of myofiber cross-sectional area (CSA) was
527 determined using the ImageJ software. Antibodies used in immunofluorescence are listed in
528 Supplementary Table 2.
529
530 **Mitochondrial morphology analysis**
531 C2C12 myoblasts were fixed with 4% paraformaldehyde at RT for 20 min, and
532 permeabilized with 0.1% Triton-X in PBS at RT for 10 min. After blocking in 3% BSA in PBS
533 for 1h, cells were incubated with TOM20 monoclonal antibody (Cell signaling technology) at
534 4°C overnight, followed by incubation with Alexa Fluor™ 488 secondary antibody (Thermo
535 Fisher). Approximately 100 mitochondria per cell were analyzed from a total of 10–15 cells,
536 resulting in ~1000 mitochondria being quantified. Mitochondrial morphology was classified as
537 fragmented, intermediate, or tubular. Mitochondria were considered 'fragmented' if the total
538 branch length was <2 μm, 'intermediate' if between 2–4 μm, and 'tubular' if >4 μm.
539 Quantification was analyzed using ImageJ software. Antibodies used in mitochondrial
540 morphology analysis are listed in Supplementary Table 2.
541
542 **Histology**
543 For SDH staining, muscle sections were incubated in 0.2 M sodium phosphate buffer
544 solution (pH 7.6) containing 0.6 mM nitro tetrazolium and 50 mM sodium succinate at 37°C
545 for 30 min. Muscle sections were washed with DiH_2O and mounted using Vectashield Hardset
546 Antifade Mounting Medium (Vector Laboratories). For modified Gomori trichrome staining,
547 frozen muscle tissues were sequentially incubated with hematoxylin and Gomori trichrome
548 staining solution (0.6% chromotrope 2R, 0.3% fast green FCF, 0.6% phosphotungstic acid, and
549 1% acetic acid), followed by dehydration through alcohol, clearing in xylene and mounting
550 with DPX mountant (Sigma-Aldrich, 6522). For H&E staining, 10 μm thick sections were

551 stained using hematoxylin and eosin, dehydrated, cleared, and mounted using DPX mountant
552 (Sigma-Aldrich). Histological images were acquired using the Leica DM750 optical
553 microscope (Leica).
554
555 **Primary myoblast isolation and culture**
556 The primary myoblasts were isolated from 3-month-old Floxed and SMKO mice
557 skeletal muscle. Skeletal muscles were minced and digested in DMEM containing 400 U ml^{-1}
558 collagenase type II (Gibco, Thermo Fisher, 17101015), 2.5% HEPES at 37°C for 1 h, with a 5-
559 second vortex halfway through. To stop digestion, cells were re-suspended in DMEM with 10%
560 FBS after centrifugation at 1,400 × g for 5 min and filtered through a 70 μm and 30 μm strainer.
561 After another centrifugation, cells were re-suspended in Ham's F-10 (Sigma Aldrich, N6908)
562 containing 20% FBS, 10 ng ml^{-1} basic fibroblast growth factor (bFGF) (Miltenyi Biotec, 130-
563 093-840), and 100 U ml^{-1} penicillin and 100 μg ml^{-1} streptomycin and plated on a Matrigel-
564 coated dish. After 72 h, primary myoblasts were purified through pre-plating for 45 min; the
565 process was repeated until fibroblasts were removed. Primary myoblasts were passaged after
566 reaching 60% confluency.
567
568 **Single myofiber isolation**
569 Gastrocnemius muscle (GA) was dissected and enzymatically digested using 0.2%
570 type I collagenase (Gibco, Thermo Fisher, 17018029) for 90 min in a shaking incubator at 37°C.
571 Digested muscles were placed onto a 10 cm dish containing DMEM with 10% FBS to stop the
572 digestion. The single myofibers were released by pipetting and washed with DMEM with 10%
573 FBS. Isolated fresh single myofibers were collected for Seahorse analysis.
574
575 **Mitochondrial isolation**
576 The Mitochondria Isolation kit for Cultured Cells or Tissue (Thermo Fisher, 89874,
577 89801) was used to isolate mitochondria from C2C12 myoblast cells or Quadriceps (Quad)
578 muscle. The experiment was performed following the manufacturer's protocol. In brief, C2C12
579 myoblasts or Quad muscle were homogenized in Reagent A using Dounce homogenizer. Then,
580 Reagents C was added sequentially, and the solution was mixed by inverting. After
581 centrifugation at 700 × g for 10 min, the supernatant was transferred to a new tube and
582 centrifuged at 3,000 × g for 15 min. Pellets were washed with Wash buffer and centrifuged at
583 12,000 × g for 5 min. All centrifugation steps were performed at 4°C. Pellets were lysed using

584 RIPA lysis buffer containing protease and phosphatase inhibitors for immunoblotting.
585
586 **Seahorse analysis**
587 To measure the oxygen consumption rate (OCR), cells or single myofibers were seeded
588 into XF96 microplates. One day after plating, the culture medium was changed to an assay
589 medium containing 1 mM pyruvate (Agilent, 103578-100), 2 mM glutamine (Agilent, 103579-
590 100), and 10 mM glucose (Agilent, 103577-100) and incubated in a CO_2-free incubator 1 h
591 before the assay began. The OCR was measured following injections of oligomycin (1.5 μM)
592 (Sigma Aldrich, O4876), FCCP (1 μM) (Sigma Aldrich, C2920), and rotenone/antimycin A (0.5
593 μM) (Sigma Aldrich, A8674, R8875). To evaluate the extracellular acidification rate (ECAR),
594 C2C12 cells were seeded into XF96 microplates. One day after plating, the culture medium
595 was changed to an assay medium containing 2 mM glutamine and incubated in a CO_2-free
596 incubator one hour before the assay began. ECAR was measured following injections of d-
597 glucose (10 mM) (Sigma Aldrich, G7528), oligomycin (1 μM), and 2-deoxy-d-glucose (50 mM)
598 (Sigma Aldrich, D8375).
599
600 **ATP contents**
601 ATP contents were determined according to the instructions for the ATPlite
602 Luminescence Assay System (PerkinElmer, 6016943). In brief, 10 μl of tissue lysates were
603 added into each well with 50 μl of the substrate solution. After shaking in the dark for 15 min,
604 luminescence intensity was measured using BioTek Synergy TM HTX Multi-Mode Microplate
605 Reader (BioTek) and normalized to the protein concentration.
606
607 **Plasma lactate measurements**
608 Whole blood was collected following cardiac puncture, and the plasma was separated
609 by centrifugation. Lactate levels in the plasma were measured using an EZ-Lactate Assay kit
610 (DoGENBio).
611
612 **Indirect calorimetry**
613 Energy expenditure was assessed using the OxyletPro Physiocage system (Panlab) and
614 METABOLISM V3.0 software (Panlab). Mice were individually housed in a metabolic
615 chamber where oxygen consumption (VO_2) and carbon dioxide production (VCO_2) were
616 continuously measured over 24 h. VO_2 and VCO_2 were measured using indirect calorimetry

617 during the experimental period. Energy expenditure was calculated by determining the
618 respiratory quotient from the recorded VO_2 and VCO_2 values.

619

620 **Proteomics analysis**

621 The tissue was frozen in liquid nitrogen and was pulverized using cryoPREP™ CPO_2
622 (Covaris). The samples were suspended in lysis buffer (8 M urea, 0.1 M Tris–HCl buffer, pH
623 8.5) and protease inhibitor cocktail, followed by sonication at 15°C for 20 min using a Covaris
624 S2 Focused-Ultrasonicator (Covaris). The Pierce BCA Protein Assay kit (Thermo Fisher) was
625 used to quantify the protein concentration. The digestion step was performed using Filter-Aided
626 Sample Preparation (FASP) on a Microcon 30K centrifugal filter device (Millipore). Each
627 sample was reduced by incubating with Tris (2-carboxyethyl)phosphine (TCEP) at 37°C for 30
628 min and alkylated with iodoacetic acid (IAA) at 25°C in dark conditions for one hour. Then,
629 after washing with lysis buffer and 50 mM ammonium bicarbonate (ABC) sequentially, the
630 proteins were digested with trypsin (enzyme to protein ratio of 1:50; w/w) at 37°C for 18 h.
631 The resulting peptide mixtures were collected in new tubes, and trypsin was inactivated by
632 acidifying with 15 µl of formic acid (Honeywell). The digested peptides were desalted using
633 C18 spin columns (Harvard Apparatus), and the peptides were eluted with 80% acetonitrile in
634 0.1% formic acid in water. The prepared samples were resuspended in 0.1% formic acid in
635 water and analyzed using a Q-Exactive Orbitrap hybrid mass spectrometer (Thermo Fisher)
636 and an Ultimate 3000 system (Thermo Fisher). We used a 2 cm × 75 µm ID trap column packed
637 with 3 µm C18 resin and a 50 cm × 75 µm ID analytical column packed with 2 µm C18 resin
638 to peptides depending on the hydrophobicity of the peptides. The mobile phase solvents
639 consisted of (A) 0.1% formic acid in water and (B) 0.1% formic acid in 90% acetonitrile, and
640 the flow rate was fixed at 300 nl min^{-1}. The gradient of the mobile phase was as follows: 4%
641 solvent B for 14 min, 4–15% solvent B for 61 min, 15–28% solvent B for 50 min, 28–40%
642 solvent B for 20 min, 40–96% solvent B for 2 min, holding at 96% of solvent B for 13 min,
643 96–4% solvent B for 1 min, and 4% solvent B for 24 min. A data-dependent acquisition method
644 was adopted, and the top 10 precursor peaks were selected and isolated for fragmentation. Ions
645 were scanned in high resolution (70,000 in MS1, 17,500 in MS2 at *m/z* 400), and the MS scan
646 range was 400–2000 *m/z* at both the MS1 and MS2 levels. Precursor ions were fragmented
647 using 27% NCE (normalized collisional energy). Dynamic exclusion was set to 30 s. Thermo
648 MS/MS raw files of each analysis were searched using Proteome Discoverer™ software (ver.

649 2.5), and the *Mus musculus* database was downloaded from UniProt. The appropriate consensus
650 workflow included a peptide-spectrum match (PSM) validation step and SEQUEST HT
651 process for detection as a database search algorithm. The search parameters were set up: 10
652 ppm of tolerances of precursor ion masses, 0.02 Da fragment ion mass, and a maximum of two
653 missed cleavages with trypsin enzyme. The dynamic modification on peptide sequence was as
654 follows: static carbamidomethylation of cysteine (+57.012 Da), variable modifications of
655 methionine oxidation (+15.995 Da), acetylation of protein N-term (+42.011 Da), and
656 carbamylation of protein in N-term (+43.0006 Da). After searching, the data results below 1%
657 of the FDR were selected and filtered using at least 6 more peptide lengths. All proteomics raw
658 data are shown in Supplementary Table 3-7.

659

660 **Transmission electron microscopy (TEM)**

661 Skeletal muscle tissues were fixed in 2.5% glutaraldehyde in 0.1 M phosphate buffer
662 (pH 7.4) and post-fixed with 1% osmium tetroxide at 4°C for 2 h. Tissues were then dehydrated
663 in an ethanol and propylene oxide series and embedded in Epon 812. Polymerization was
664 conducted using pure resin at 70°C for two days. Ultrathin sections (70 nm) were cut using an
665 UltraCut-UCT ultramicrotome (Leica) and placed on 150-mesh copper grids. After staining
666 using 2% uranyl acetate and lead citrate, the sections were observed at 120 kV by FEI Tecnai
667 G^2 Spirit Twin transmission electron microscopy (FEI).

668

669 **In vitro copper binding assay**

670 In total, 1 μg of recombinant GST-MTCH2 or 100 μg of cell lysates were incubated in
671 500 μl of RIPA containing 50 μl Profinity IMAC resin (Bio-Rad, 1560123) charged with no
672 metal, Cu^{2+}, Fe^{2+}, Zn^{3+}, or copper-chelating resin (G-Biosciences, 786-285) at 4°C for 1 h with
673 rotation. After 3 washes using RIPA buffer, immunoblotting was performed as described above.

674

675 **DNA constructs and site-directed mutagenesis**

676 pCMV3-MTCH2-myc was purchased from SinoBiological (SinoBiological,
677 HG16436-CM). Point mutations were generated in *Mtch2* using a Q5®Site-Directed

678 Mutagenesis kit (New England Biolabs, EZ004S) with primers shown in Supplementary Table
679 1. All constructs were confirmed by DNA sequencing.

680

681 **Prediction of MTCH2 three-dimensional structure and copper-binding amino acid**
682 **residues**

683 The three-dimensional structure of MTCH2 was modeled using AlphaFold3
684 (https://alphafoldserver.com/). The modeled MTCH2 structure was predicted through a
685 structural similarity search (Liisa Holm, http://ekhidna2.biocenter.helsinki.fi/dali), comparing
686 it with the mitochondrial brown fat uncoupling protein (PDB ID 8J1N) and mitochondrial
687 ADP/ATP carrier proteins (PDB IDs 1OKC and 4C9H), yielding Z-scores higher than 20[37,38].
688 Using these structures as templates, copper-binding sites in MTCH2 were modeled through
689 SWISS MODEL[39]. Based on the presence of methionine (M), cysteine (C), and histidine (H)
690 residues, which are commonly observed in copper ion-binding proteins, regions rich in sulfur
691 atoms outside the α-barrel (M244, M278, C268) and regions rich in nitrogen and oxygen atoms
692 inside the α-barrel (H142, R185, S241; H88, E127, R131) were selected as potential copper-
693 binding sites in human MTCH2.

694

695 **Bioinformatic analysis**

696 To examine the gene expression levels of *Ctr1* in the skeletal muscle of normal and
697 mitochondrial myopathy patients, the Gene Expression Omnibus (GEO) dataset (GSE43698)
698 was accessed. In brief, transcript profiling was obtained from skeletal muscle samples of 4
699 normal and 11 mitochondrial myopathy individuals.

700

701 **Statistical analysis**

702 Data are presented as the mean ± SEM. A two-tailed, unpaired Student's t-test was
703 used for pairwise comparison of treatments. One-way ANOVA and two-ANOVA, followed by
704 Tukey's or Šídák's multiple comparisons test, were used to compare three or more groups, as
705 indicated in the figure legends. Analysis was performed using the statistical software package
706 Prism 10.0 (GraphPad Software). Differences were considered significant at $p < 0.05$.

Data availability

The mass spectrometry proteomics data have been deposited to the ProteomeXchange Consortium via the PRIDE partner repository with the dataset identifier PXD064414. The RNAseq data used in this study for the analysis of *CTR1* expression (Fig. 3i) from the skeletal muscle of normal and mitochondrial myopathy patients are available from GSE43698.

Code availability

All analyses were performed using standard software packages as described in the Methods.

REFERENCES

1 Tapiero, H., Townsend, D. M. & Tew, K. D. Trace elements in human physiology and pathology. Copper. *Biomed. Pharmacother.* **57**, 386-398 (2003).

2 Ruiz, L. M., Libedinsky, A. & Elorza, A. A. Role of Copper on Mitochondrial Function and Metabolism. *Front. Mol. Biosci.* **8**, 711227 (2021).

3 Bost, M. *et al.* Dietary copper and human health: Current evidence and unresolved issues. *J. Trace Elem. Med. Biol.* **35**, 107-115 (2016).

4 Chun, H., Catterton, T., Kim, H., Lee, J. & Kim, B. E. Organ-specific regulation of ATP7A abundance is coordinated with systemic copper homeostasis. *Sci Rep* **7**, 12001 (2017).

5 Kim, B.-E., Nevitt, T. & Thiele, D. J. Mechanisms for copper acquisition, distribution and regulation. *Nat. Chem. Biol.* **4**, 176-185 (2008).

6 La Fontaine, S. & Mercer, J. F. Trafficking of the copper-ATPases, ATP7A and ATP7B: role in copper homeostasis. *Arch Biochem Biophys* **463**, 149-167 (2007).

7 Liu, Y., Pilankatta, R., Hatori, Y., Lewis, D. & Inesi, G. Comparative features of copper ATPases ATP7A and ATP7B heterologously expressed in COS-1 cells. *Biochemistry* **49**, 10006-10012 (2010).

8 Nose, Y., Kim, B. E. & Thiele, D. J. Ctr1 drives intestinal copper absorption and is essential for growth, iron metabolism, and neonatal cardiac function. *Cell Metab.* **4**, 235-244 (2006).

9 Kim, B. E. *et al.* Cardiac copper deficiency activates a systemic signaling mechanism that communicates with the copper acquisition and storage organs. *Cell Metab.* **11**, 353-363 (2010).

10 Frontera, W. R. & Ochala, J. Skeletal muscle: a brief review of structure and function. *Calcif. Tissue Int.* **96**, 183-195 (2015).

11 Mukund, K. & Subramaniam, S. Skeletal muscle: A review of molecular structure and function, in health and disease. *Wiley Interdiscip. Rev. Syst. Biol. Med.* **12**, e1462 (2020).

12 Schiaffino, S. & Reggiani, C. Fiber types in mammalian skeletal muscles. *Physiol. Rev.* **91**, 1447-1531 (2011).

13 Pette, D. & Staron, R. S. Mammalian skeletal muscle fiber type transitions. *Int. Rev. Cytol.* **170**, 143-223 (1997).

14 Song, M. Y. *et al.* Sirt6 reprograms myofibers to oxidative type through CREB-dependent Sox6 suppression. *Nat. Commun.* **13**, 1808 (2022).

15 Wen, W. *et al.* Lycopene increases the proportion of slow-twitch muscle fiber by AMPK signaling to improve muscle anti-fatigue ability. *J. Nutr. Biochem.* **94**, 108750 (2021).

16 Pereira, C. V. *et al.* Myopathy reversion in mice after restauration of mitochondrial complex I. *EMBO Mol. Med.* **12**, e10674 (2020).

17 Diaz, F., Thomas, C. K., Garcia, S., Hernandez, D. & Moraes, C. T. Mice lacking COX10 in skeletal muscle recapitulate the phenotype of progressive mitochondrial myopathies associated with cytochrome c oxidase deficiency. *Hum. Mol. Genet.* **14**, 2737-2748 (2005).

18 Tsukihara, T. *et al.* Structures of Metal Sites of Oxidized Bovine Heart Cytochrome c Oxidase at 2.8 Å. *Science* **269**, 1069-1074 (1995).
19 Leary, S. C., Winge, D. R. & Cobine, P. A. "Pulling the plug" on cellular copper: the role of mitochondria in copper export. *Biochim Biophys Acta* **1793**, 146-153 (2009).
20 Bustos, R. I. *et al.* Copper deficiency alters cell bioenergetics and induces mitochondrial fusion through up-regulation of MFN2 and OPA1 in erythropoietic cells. *Biochem. Biophys. Res. Commun.* **437**, 426-432 (2013).
21 Squitti, R. & Polimanti, R. Copper phenotype in Alzheimer's disease: dissecting the pathway. *Am J Neurodegener Dis* **2**, 46-56 (2013).
22 Fujisawa, C. *et al.* Early clinical signs and treatment of Menkes disease. *Molecular Genetics and Metabolism Reports* **31**, 100849 (2022).
23 Vest, K. E., Paskavitz, A. L., Lee, J. B. & Padilla-Benavides, T. Dynamic changes in copper homeostasis and post-transcriptional regulation of Atp7a during myogenic differentiation. *Metallomics* **10**, 309-322 (2018).
24 McCann, C. *et al.* The mitochondrial Cu(+) transporter PiC2 (SLC25A3) is a target of MTF1 and contributes to the development of skeletal muscle in vitro. *Front. Mol. Biosci.* **9**, 1037941 (2022).
25 Gregory, C. M., Vandenborne, K. & Dudley, G. A. Metabolic enzymes and phenotypic expression among human locomotor muscles. *Muscle & Nerve* **24**, 387-393 (2001).
26 Chennamsetty, I. *et al.* Nat1 Deficiency Is Associated with Mitochondrial Dysfunction and Exercise Intolerance in Mice. *Cell Rep.* **17**, 527-540 (2016).
27 Brischigliaro, M. & Zeviani, M. Cytochrome c oxidase deficiency. *Biochim. Biophys. Acta Bioenerg.* **1862**, 148335 (2021).
28 Furukawa, Y., Torres, A. S. & O'Halloran, T. V. Oxygen-induced maturation of SOD1: a key role for disulfide formation by the copper chaperone CCS. *EMBO J.* **23**, 2872-2881 (2004).
29 Bertinato, J. & L'Abbé, M. R. Copper modulates the degradation of copper chaperone for Cu,Zn superoxide dismutase by the 26 S proteosome. *J. Biol. Chem.* **278**, 35071-35078 (2003).
30 Ryzhkova, A. I. *et al.* Mitochondrial diseases caused by mtDNA mutations: a mini-review. *Ther. Clin. Risk Manag.* **14**, 1933-1942 (2018).
31 Ahmed, S. T., Craven, L., Russell, O. M., Turnbull, D. M. & Vincent, A. E. Diagnosis and Treatment of Mitochondrial Myopathies. *Neurotherapeutics* **15**, 943-953 (2018).
32 Aptekmann, A. A. *et al.* mebipred: identifying metal-binding potential in protein sequence. *Bioinformatics* **38**, 3532-3540 (2022).
33 Goldman, A. *et al.* MTCH2 cooperates with MFN2 and lysophosphatidic acid synthesis to sustain mitochondrial fusion. *EMBO Rep.* **25**, 45-67 (2024).
34 Grinberg, M. *et al.* Mitochondrial carrier homolog 2 is a target of tBID in cells signaled to die by tumor necrosis factor alpha. *Mol Cell Biol* **25**, 4579-4590 (2005).
35 Buzaglo-Azriel, L. *et al.* Loss of Muscle MTCH2 Increases Whole-Body Energy Utilization and Protects from Diet-Induced Obesity. *Cell Rep.* **18**, 1335-1336 (2017).
36 Guna, A. *et al.* MTCH2 is a mitochondrial outer membrane protein insertase. *Science* **378**, 317-322 (2022).
37 Kang, Y. & Chen, L. Structural basis for the binding of DNP and purine nucleotides onto UCP1. *Nature* **620**, 226-231 (2023).
38 Pebay-Peyroula, E. *et al.* Structure of mitochondrial ADP/ATP carrier in complex with carboxyatractyloside. *Nature* **426**, 39-44 (2003).
39 Waterhouse, A. *et al.* SWISS-MODEL: homology modelling of protein structures and complexes. *Nucleic Acids Res.* **46**, W296-w303 (2018).
40 Forrest, I. *et al.* Proteome-Wide Discovery of Degradable Proteins Using Bifunctional Molecules. *bioRxiv*, 2025.2003.2021.644652 (2025).
41 Bahat, A. *et al.* MTCH2-mediated mitochondrial fusion drives exit from naïve pluripotency in embryonic stem cells. *Nat. Commun.* **9**, 5132 (2018).
42 Yoneshiro, T. *et al.* BCAA catabolism in brown fat controls energy homeostasis through SLC25A44. *Nature* **572**, 614-619 (2019).

43 Verkerke, A. R. P. *et al.* SLC25A48 controls mitochondrial choline import and metabolism. *Cell Metabolism* **36**, 2156-2166.e2159 (2024).
44 Nose, Y. *et al.* Ctr1 Is an Apical Copper Transporter in Mammalian Intestinal Epithelial Cells in Vivo That Is Controlled at the Level of Protein Stability*. *J. Biol. Chem.* **285**, 32385-32392 (2010).
45 Soma, S. *et al.* Elesclomol restores mitochondrial function in genetic models of copper deficiency. *Proc. Natl Acad. Sci. USA* **115**, 8161-8166 (2018).
46 Yuan, S., Korolnek, T. & Kim, B. E. Oral Elesclomol Treatment Alleviates Copper Deficiency in Animal Models. *Front. Cell Dev. Biol.* **10**, 856300 (2022).
47 Guthrie, L. M. *et al.* Elesclomol alleviates Menkes pathology and mortality by escorting Cu to cuproenzymes in mice. *Science* **368**, 620-625 (2020).
48 Hood, D. A., Memme, J. M., Oliveira, A. N. & Triolo, M. Maintenance of Skeletal Muscle Mitochondria in Health, Exercise, and Aging. *Annu. Rev. Physiol.* **81**, 19-41 (2019).
49 Cobine, P. A., Moore, S. A. & Leary, S. C. Getting out what you put in: Copper in mitochondria and its impacts on human disease. *Biochim. Biophys. Acta Mol. Cell Res.* **1868**, 118867 (2021).
50 Boulet, A. *et al.* The mammalian phosphate carrier SLC25A3 is a mitochondrial copper transporter required for cytochrome c oxidase biogenesis. *J. Biol. Chem.* **293**, 1887-1896 (2018).
51 Xu, W., Barrientos, T. & Andrews, N. C. Iron and copper in mitochondrial diseases. *Cell Metab.* **17**, 319-328 (2013).
52 Murata, D., Roy, S., Lutsenko, S., Iijima, M. & Sesaki, H. Slc25a3-dependent copper transport controls flickering-induced Opa1 processing for mitochondrial safeguard. *Developmental Cell* **59**, 2578-2592.e2577 (2024).
53 Chourasia, S. *et al.* MTCH2 controls energy demand and expenditure to fuel anabolism during adipogenesis. *EMBO J.* **44**, 1007-1038 (2025).
54 Grevendonk, L. *et al.* Impact of aging and exercise on skeletal muscle mitochondrial capacity, energy metabolism, and physical function. *Nat. Commun.* **12**, 4773 (2021).
55 Allodi, I., Montañana-Rosell, R., Selvan, R., Löw, P. & Kiehn, O. Locomotor deficits in a mouse model of ALS are paralleled by loss of V1-interneuron connections onto fast motor neurons. *Nat. Commun.* **12**, 3251 (2021).
56 Białobrodzka, E. *et al.* Amyotrophic Lateral Sclerosis and swim training affect copper metabolism in skeletal muscle in a mouse model of disease. *Muscle & Nerve* **70**, 1111-1118 (2024).
57 Ogbonmide, T. *et al.* Gene Therapy for Spinal Muscular Atrophy (SMA): A Review of Current Challenges and Safety Considerations for Onasemnogene Abeparvovec (Zolgensma). *Cureus* **15**, e36197 (2023).
58 Mendell, J. R. *et al.* Current Clinical Applications of In Vivo Gene Therapy with AAVs. *Mol. Ther.* **29**, 464-488 (2021).
59 Mah, C. S. *et al.* Adeno-associated virus-mediated gene therapy for metabolic myopathy. *Hum. Gene. Ther.* **24**, 928-936 (2013).

Acknowledgements

This work was supported by the National Research Foundation of Korea (NRF) grants (RS-2021-NR058898 and RS-2023-00219517) and the Main Research Program (E0210103) of the Korea Food Research Institute, all funded by the Korea government (MSIT), in addition to support from the National Institutes of Health (Grant ID: R01 DK129599 to Byung-Eun Kim).

856 **Author contributions**

857 Y.-S.L. and H.-S.K. designed and performed experiments, analyzed and interpreted data, and
858 wrote the manuscript; P.L.N. conducted bioinformatics analysis; J.L. and D.-I.K. generated
859 *Ctr1*-AAV; J.L. and C.M. performed histological analysis; K.-O.C., B.-E.K., T.F.O., and J.A.
860 analyzed and interpreted data and critically reviewed the manuscript; T.D. performed modeling;
861 J.-S.K., C.H.J., and T.-I.J. conceived and designed the experiments and wrote the manuscript;
862 All authors reviewed and edited the manuscript.

863

864 **Competing interests**

865 Kyoung-Oh Cho is a board member of Pharmacolinx Inc. All other authors declare no
866 competing interests.

867

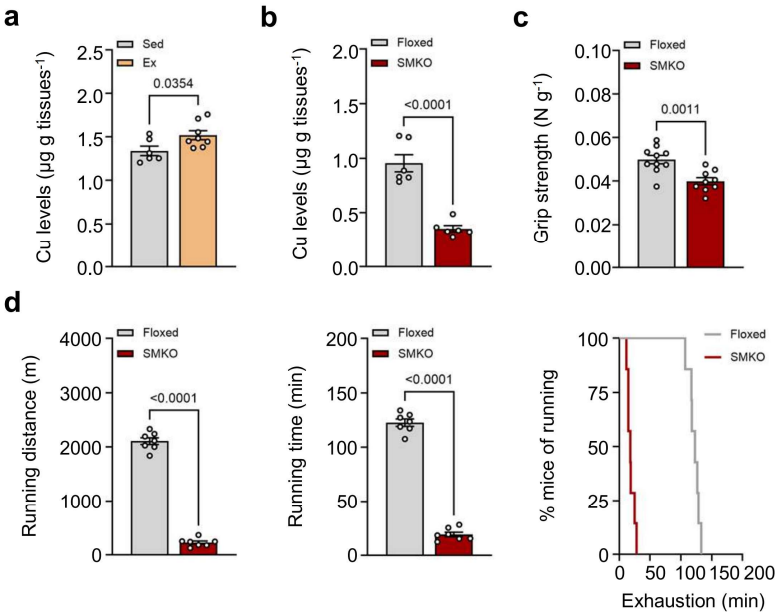

Fig. 1 Copper uptake induced by exercise supports skeletal muscle performance in mice. **a,b,** Copper levels in the GA skeletal muscle of exercise-trained wild-type (**a**) and SMKO (**b**) mice (n = 6–8). **c,** Forelimb grip strength of Floxed and SMKO mice (n = 9–10). **d,** Running distance, running time, and exhaustion rate of Floxed and SMKO mice in treadmill training (n = 7). Data are presented as mean ± SEM. Statistical differences were determined by two-tailed Student's t-test.

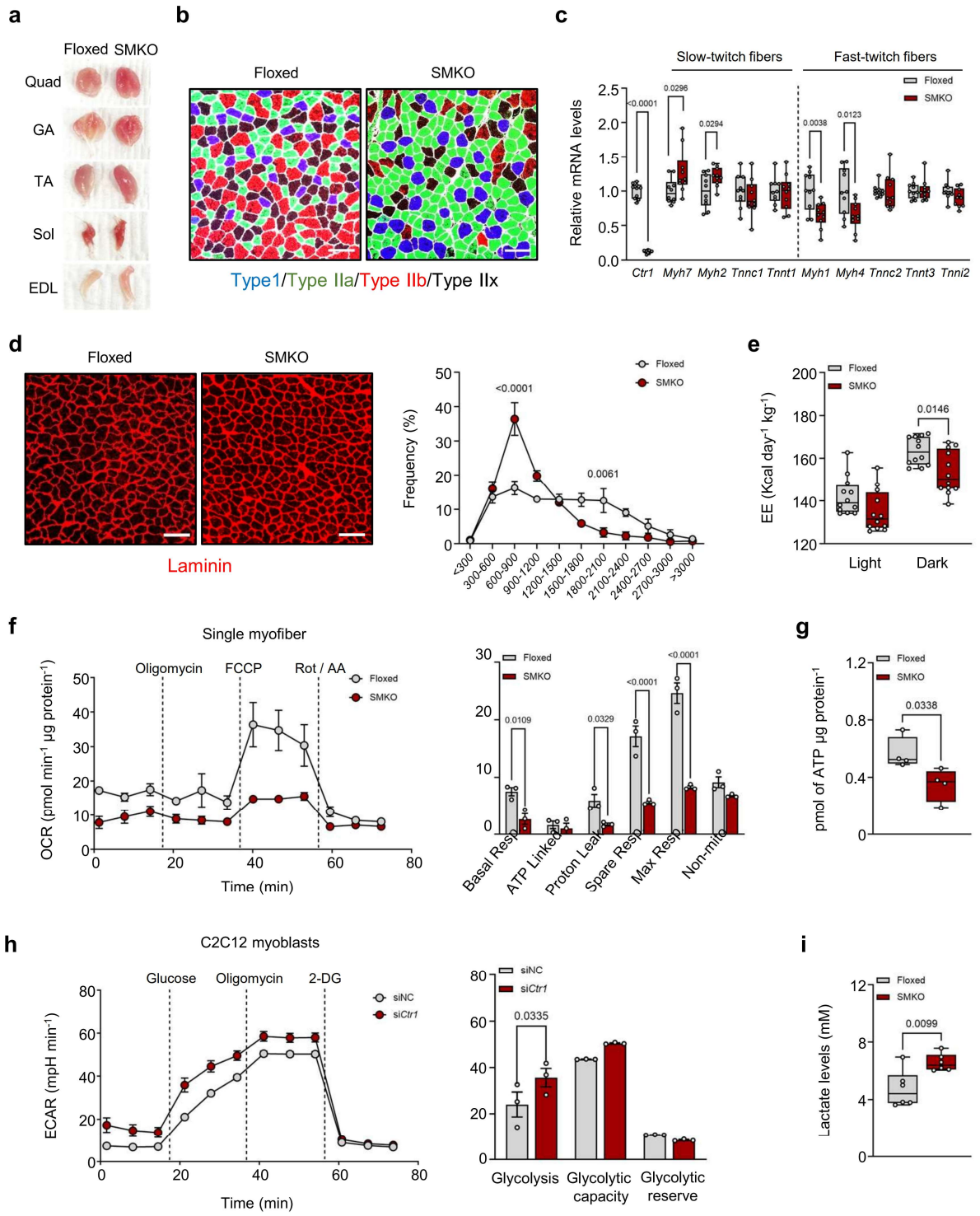

Fig. 2 Glycolytic adaptation and reduced energy expenditure in SMKO mice with skeletal muscle copper deficiency. a, Representative images of skeletal muscle from Floxed and SMKO mice. **b,** Immunofluorescence staining of myofiber types in the GA muscles of Floxed and SMKO mice. Scale bars = 100 µm. **c,** mRNA expression of slow- and fast-twitch fiber-related genes in the GA muscle of Floxed and SMKO mice (n = 10). **d,** Cross-sectional area (CSA) of each myofiber in the GA muscle of Floxed and SMKO mice. CSA frequency was calculated using ImageJ. Scale bars = 100 µm. **e,** Energy expenditure of Floxed and SMKO

886 mice. **f,** Oxygen consumption rate (OCR) of single myofibers isolated from the GA muscle of
887 Floxed and SMKO mice following sequential treatment with oligomycin (Oligo), carbonyl
888 cyanide p-triflouromethoxyphenylhydrazone (FCCP), rotenone (Rot), and antimycin A (AA).
889 **g,** ATP levels in GA muscles of Floxed and SMKO mice (n = 4). **h,** Extracellular acidification
890 rate (ECAR) of C2C12 myoblasts after *Ctr1* knockdown. siNC, negative control siRNA; si*Ctr1*,
891 *Ctr1* siRNA **i,** Blood lactate concentration of Floxed and SMKO mice (n = 6). Data are
892 presented as mean ± SEM. Statistical differences were determined by two-way ANOVA with
893 Šídák's multiple comparisons test (**d-f**,**h**) and two-tailed Student's t-test (**c**,**g**,**i**).
894
895

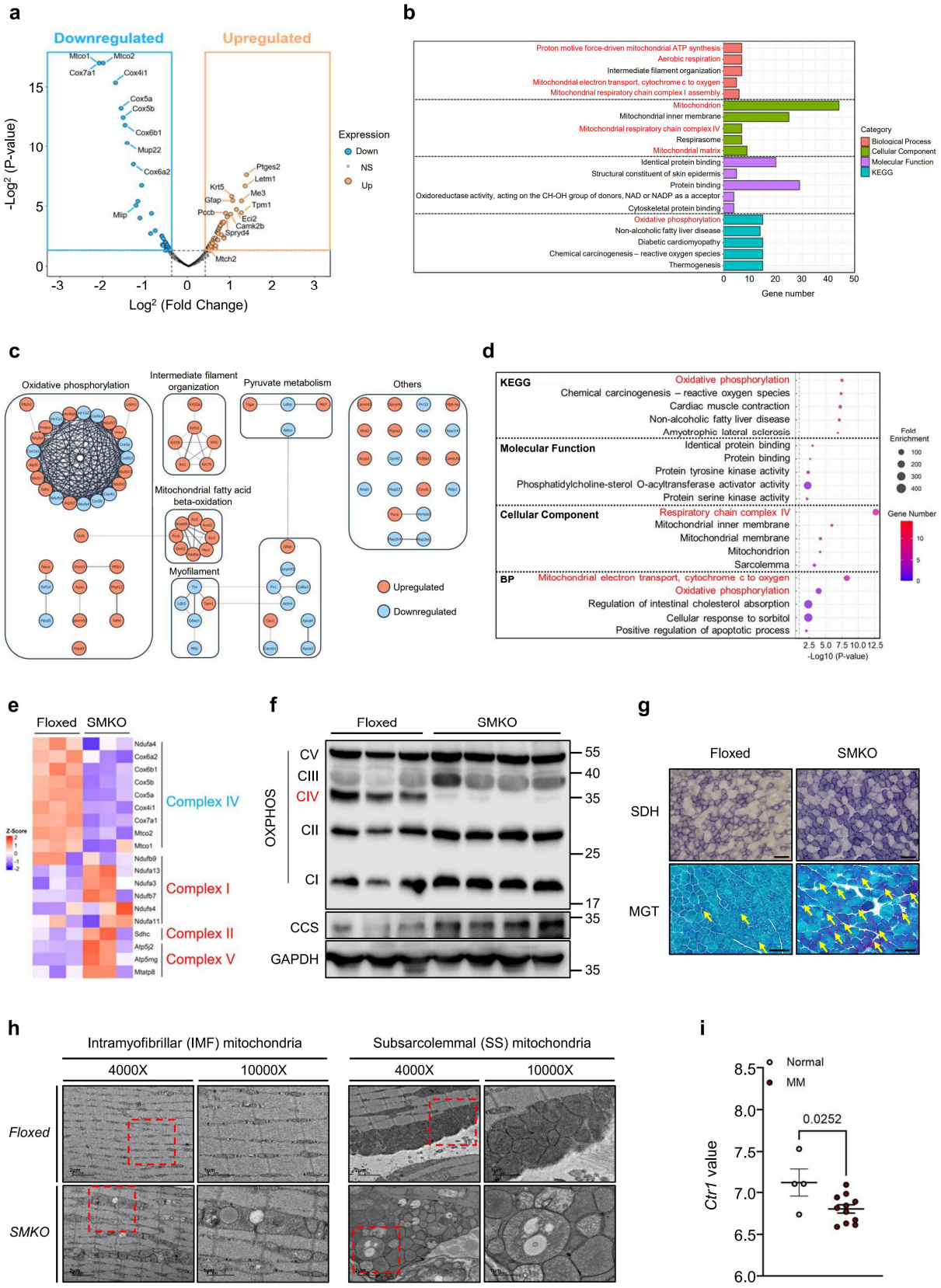

Fig. 3 Disrupted Complex IV and MM-related changes in SMKO skeletal muscle. a-d, Proteomics analysis of the GA muscle of Floxed and SMKO mice. (**a**), Volcano plot. (**b**), GO

analysis of DEPs. (**c**)**,** STRING network analysis of DEPs. (**d**)**,** GO analysis of downregulated proteins in SMKO compared to Floxed mice. **e,** Heatmap visualization of OXPHOS-related protein expression. **f-h,** Analysis of mitochondrial function in the GA muscle of Floxed and SMKO mice. (**f**)**,** Protein levels of OXPHOS components and CCS. (**g**)**,** SDH and modified Gomori trichorme (MGT) staining. Yellow arrows indicate ragged-red fibers. Scale bar = 100 μm. (**h**)**,** Transmission electron microscopy (TEM) images. Scale bar = 2 μm (4,000× magnification), 1 μm (10,000× magnification). **i,** *CTR1* expression levels of individuals with the MM compared to normal controls (extracted from GSE43698). Data are presented as mean ± SEM. Statistical differences were determined by two-tailed Student's t-test (**i**).

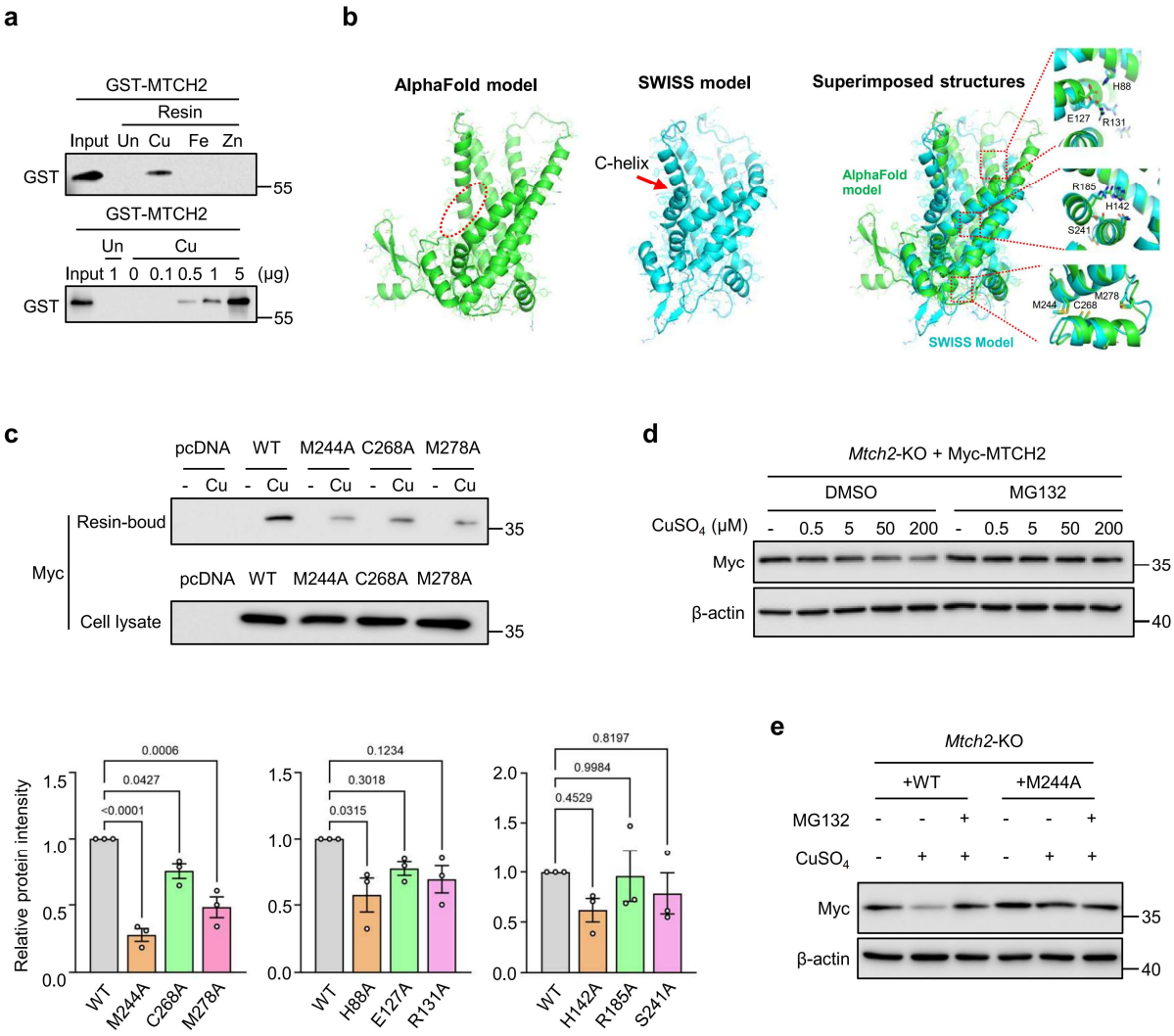

Fig. 4 MTCH2 stability is regulated by copper binding. a, *In vitro* copper-binding assay using glutathione S-transferase (GST)-tagged human recombinant MTCH2 protein. **b,** Predicted structural models of MTCH2 generated by Alphafold3 (Left panel) and SWISS-MODEL (middle panel). Predicted amino acids involved in copper binding (right panel). **c,** *In vitro* copper-binding assay using HEK293T cells overexpressing wild-type or alanine mutant pCMV3-MTCH2-Myc constructs. Protein expression was normalized to Myc levels in whole-cell lysates. n = 3 independent experiments. **d,e,** Immunoblot analysis of *Mtch2*-knockout C2C12 myoblasts re-expressing pCMV3- MTCH2-Myc-wild-type (**d**) or MTCH2-M244A (**e**), pre-treated with MG132 (1μM) for 2 h and subsequently exposed to $CuSO_4$ for 6 h. Data are presented as mean ± SEM. Statistical differences were determined by one-way ANOVA (**c**) with Tukey's test.

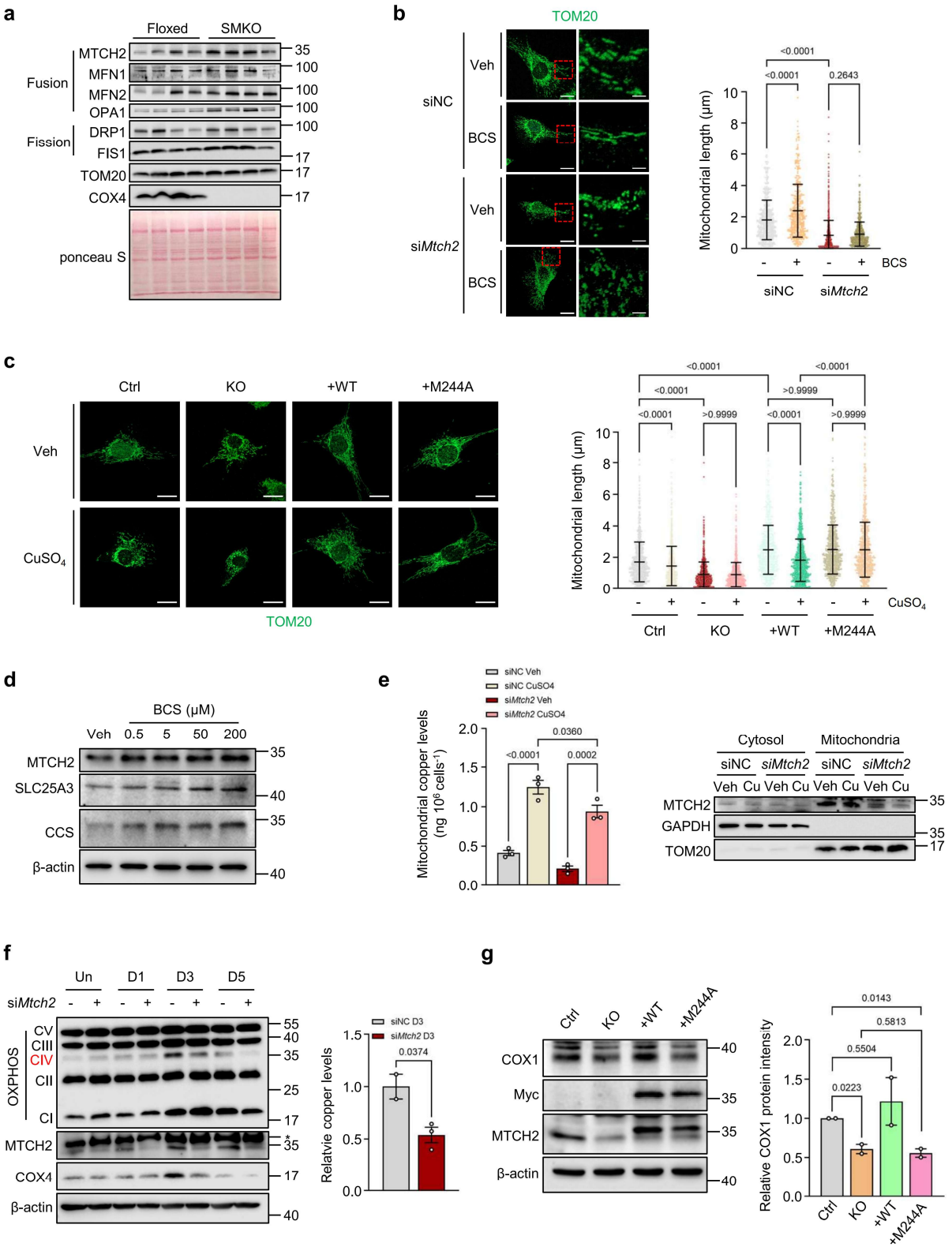

Fig. 5 MTCH2 contributes to mitochondrial dynamics and copper homeostasis a, Immunoblot analysis of mitochondria isolated from the Quad muscle of Floxed and SMKO mice. **b,c,** Immunofluorescence staining of mitochondrial morphology in BCS (50 μM) treated *Mtch2* knockdown C2C12 myoblasts (**b**), and *Mtch2* knockout C2C12 myoblasts re-expressing

MTCH2-wild-type or MTCH2-M244A treated with $CuSO_4$ (200 μM) for 6 h (**c**). Scale bars = 20 μm and 5 μm (zoomed in). Mitochondrial length was quantified from ~1,000 mitochondria observed in 10-15 cells using Image J. **d,** Immunoblot analysis of human skeletal muscle myoblasts (HSMM) treated with vehicle or BCS for 24 h. **e,** ICP-MS analysis of mitochondrial copper in *Mtch2* knockdown C2C12 myoblasts treated with or without $CuSO_4$ (50 μM) for 24 h ($n = 3$) and immunoblot analysis of cytosolic and mitochondrial fractions isolated from *Mtch2* knockdown C2C12 myoblasts. siNC, negative control siRNA; si*Mtch2*, *Mtch2* siRNA. **f,g,** Immunoblot analysis of differentiated C2C12 myoblasts following *Mtch2* knockdown (**f**), and differentiated *Mtch2* knockout C2C12 myotubes re-expressing pCMV3-MTCH2-Myc-wild-type or MTCH2-M244A treated with $CuSO_4$ (50 μM) for 24 h. COX1 protein expression was normalized to β-actin levels. $n = 2$ independent experiments. (**g**). Data are presented as mean ± SEM (**e-g**) or ± SD (**b,c**). Statistical differences were determined by two-tailed Student's t-test (**f**), one-way ANOVA (**b,c,e,g**) with Tukey's test.

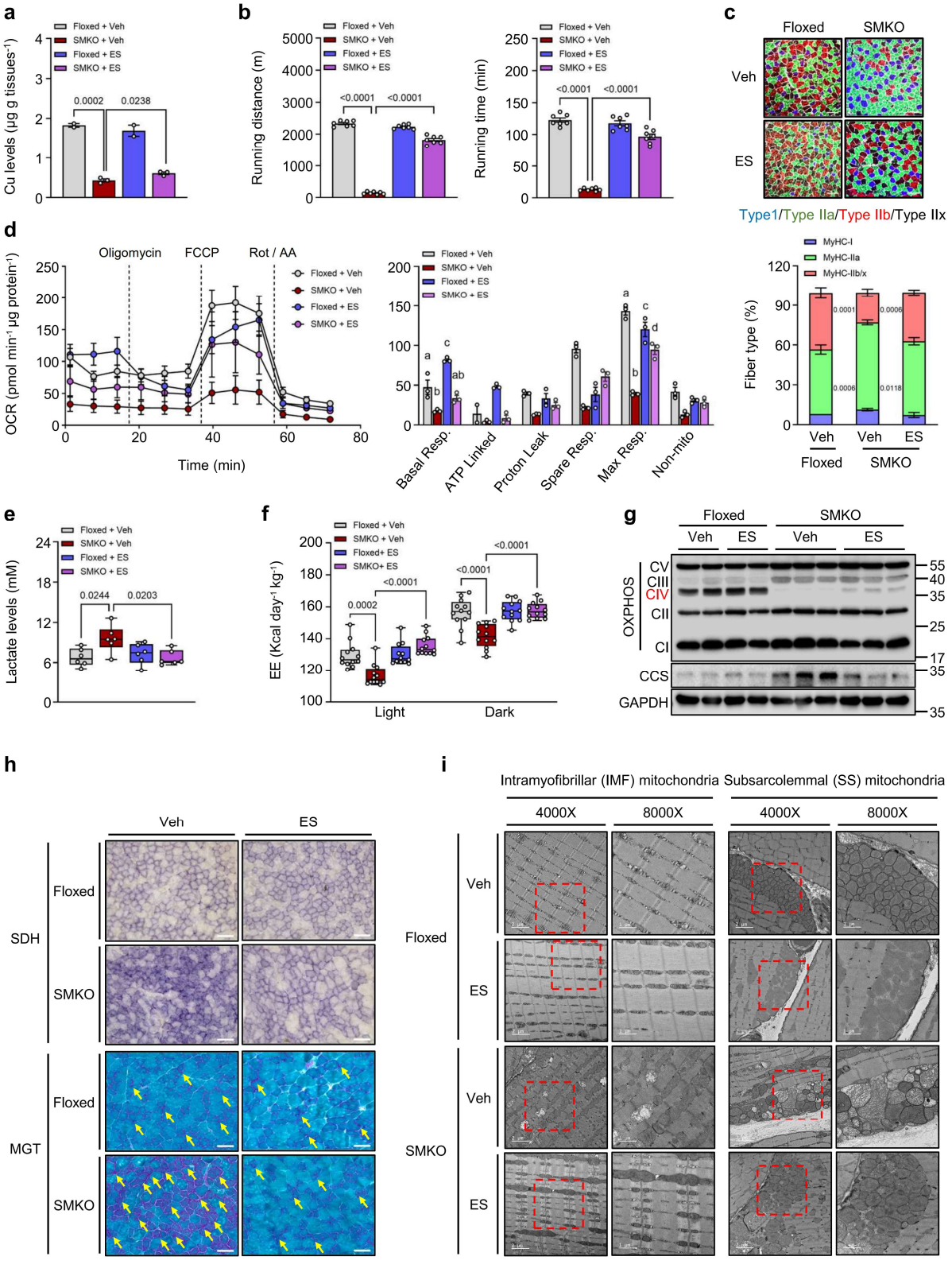

Fig. 6 ES rescues mitochondrial function, energy metabolism, and exercise capacity in SMKO mice. ES was administrated subcutaneously to Floxed and SMKO mice for 2 weeks. **a,** Copper levels in the GA muscle (n = 2–3). **b,** Running distance and duration in treadmill training (n = 7). **c,** Immunofluorescence staining of myofiber types. **d,** OCR of single myofibers.

Bars labeled with different letters (a, b, c, d) indicate statistically significant differences between groups ($p < 0.05$). **e,** Blood lactate concentration ($n = 6$). **f,** Energy expenditure ($n = 5–7$). **g,** OXPHOS and CCS protein levels. **h,** SDH and MGT staining. Scale bar = 100 μm. **i,** TEM images. Scale bar = 2 μm (4,000× magnification), 1 μm (8,000× magnification). Data are presented as mean ± SEM. Statistical differences were determined by one-way ANOVA (**a,b,e**) and two-way ANOVA (**c,d,f**) with Tukey's test.

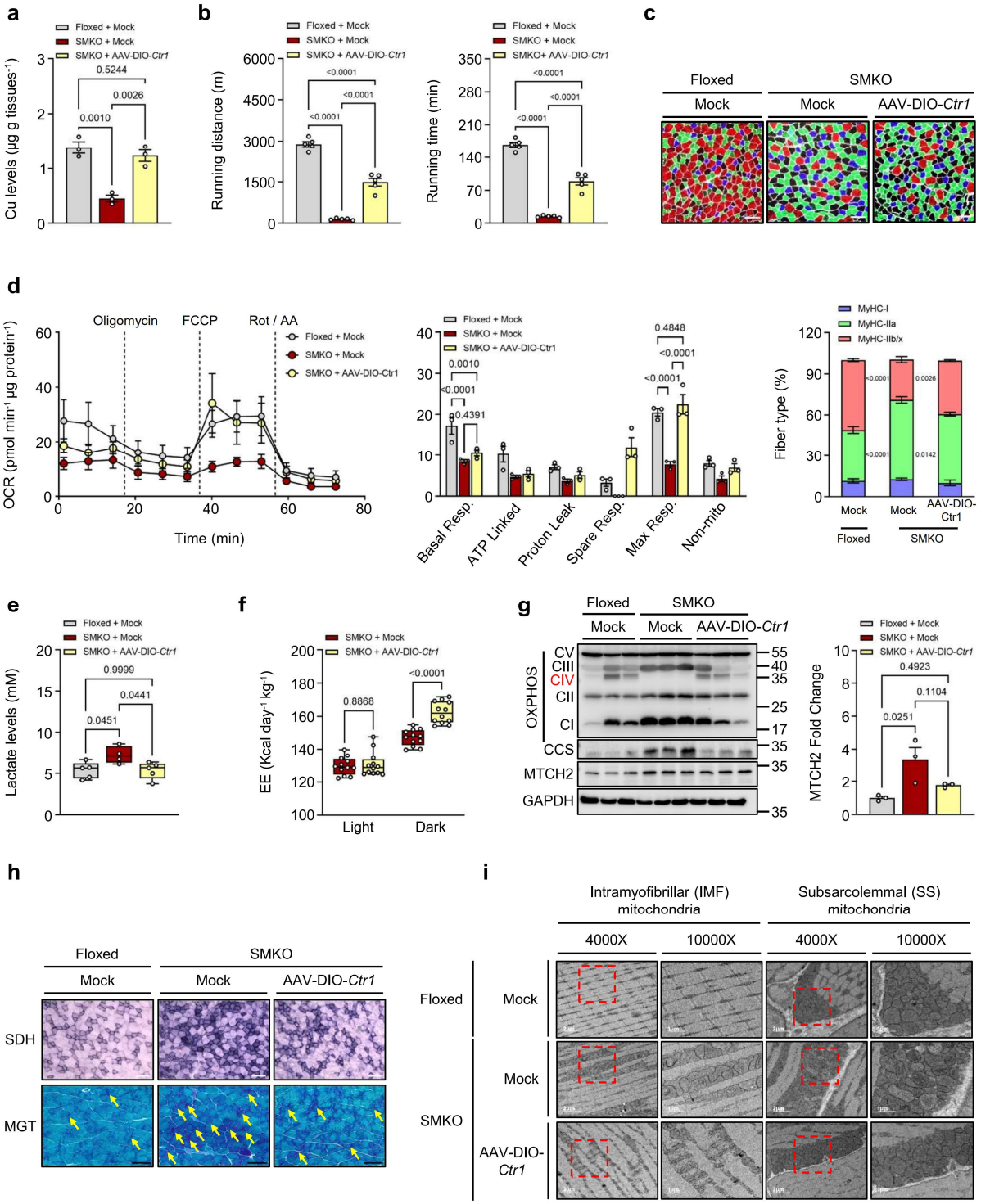

Fig. 7 AAV-DIO-mediated *Ctr1* re-expression in skeletal muscle restores mitochondrial function and improves exercise performance in SMKO mice. A single intramuscular injection of AAV-DIO-*Ctr1* was administered to SMKO mice, and assessments were performed after 5 weeks. **a,** Copper levels in the GA muscle (n = 3). **b,** Running distance and duration in treadmill training (n = 5). **c,** Immunofluorescence staining of myofiber types. **d,** OCR of single myofibers. **e,** Blood lactate concentration (n = 4–5). **f,** Energy expenditure. **g,** OXPHOS, CCS, and MTCH2 protein levels, normalized to GAPDH expression. **h,** SDH and MGT staining.

Scale bar = 100 μm. **i,** TEM images. Scale bar = 2 μm (4,000× magnification), 1 μm (10,000× magnification). Data are presented as mean ± SEM. Statistical differences were determined by one-way ANOVA (**a,b,e,g**) and two-way ANOVA with Tukey's test (**c,d**) or Šídák's multiple comparisons test (**f**). ns, not significant.